Relaxation of the Jahn–Teller stress effect in the P3-type K$_{0.5}$MnO$_2$ cathode by copper and magnesium co-substitution for high-performance K-ion batteries

Yunjae Oh [a,1], Hoseok Lee [b,c,1], Gwangeon Oh [a,1], Seongje Ryu [a], Un-Hyuck Kim [d], Hun-Gi Jung [b,e,f], Jongsoon Kim [b,c,e,f,**], Jang-Yeon Hwang [a,g,*]

[a] *Department of Energy Engineering, Hanyang University, Seoul 04763, Republic of Korea*
[b] *Department of Energy Science, Sungkyunkwan University, Suwon 16419, Republic of Korea*
[c] *SKKU Institute of Energy Science and Technology (SIEST), Sungkyunkwan University, Suwon 16419, Republic of Korea*
[d] *Department of Energy Science and Engineering, Daegu Gyeongbuk Institute of Science and Technology, Daegu 42988, Republic of Korea*
[e] *Energy Storage Research Center, Clean Energy Research Division, Korea Institute of Science and Technology, Seoul 02792, Republic of Korea*
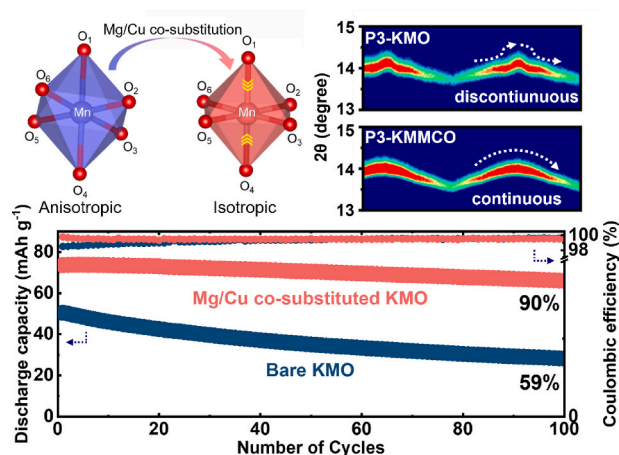[f] *KIST-SKKU Carbon-Neutral Research Center, Sungkyunkwan University, Suwon 16419, Republic of Korea*
[g] *Department of Battery Engineering, Hanyang University, Seoul 04763, Republic of Korea*

HIGHLIGHTS

- The synergy effect of Mg and Cu co-substitution suppress the Jahn-Teller distortion.
- The P3-KMMCO cathode exhibits a superior cycling stability and power capability.
- DFT calculations confirm suppression of Jahn-Teller distortion in P3-KMMCO cathode.

GRAPHICAL ABSTRACT

ARTICLE INFO

ABSTRACT

The Mn-based P3-type layered oxide (K$_{0.5}$MnO$_2$) is a promising cathode material for K-ion batteries (KIBs) because of its low cost, high specific capacity, and simple synthesis. However, it suffers from severe capacity loss and sluggish K$^+$ diffusion kinetics, which are mainly attributed to multiple phase transitions and the Jahn–Teller

---

distortion of Mn^{3+}. To address these challenges, herein, the Mg and Cu co-substitution strategy is proposed to synthesize the P3-type $K_{0.5}Mn_{0.8}Mg_{0.1}Cu_{0.1}O_2$ (P3-KMMCO) as a cathode for KIBs. The presence of divalent Mg^{2+} and Cu^{2+} in the crystal structure of P3-KMMCO play the critical functions in regulating the Jahn–Teller-active Mn^{3+}, thereby suppressing the complex phase transitions and improving the K^+ diffusion kinetics during charging and discharging. As a result, the P3-KMMCO cathode demonstrates the high reversible capacity, outstanding cycling stability and power capability. A combination study of synchrotron-based X-ray analysis and first-principles calculations is used to validate the enhanced electrochemical K^+ storage properties of the P3-KMMCO cathode.

1. Introduction

Lithium-ion batteries (LIBs) have become ubiquitous in energy storage applications ranging from portable electronic devices to large-scale energy storage systems, primarily due to their impressive energy density [1–3]. Though it is demand-driven, the price of cobalt, which is a key component in LIBs, remains vulnerable to supply, with approximately 60% of global cobalt mining occurring in the politically unstable Democratic Republic of Congo [4]. Similarly, the uneven distributions and scarcities of lithium and other key metals within Earth's crust limit the permanent availabilities of energy storage systems such as LIBs, further escalating their costs [5]. In light of these concerns, numerous researchers have explored alternative battery systems to LIBs, including Na-ion batteries (NIBs), K-ion batteries (KIBs), Zn-ion batteries, and lithium-sulfur batteries [6–11]. Among these alternatives, KIBs have attracted considerable attention due to the abundance of K resources (Li: 0.0017 wt.% *vs.* K: 2.09 wt.%) and low standard reduction potential of K^+/K (−2.936 V *vs.* the standard hydrogen electrode (SHE)). This standard reduction potential is similar to that of Li^+/Li (−3.04 V *vs.* SHE) but lower than that of Na^+/Na (−2.71 V *vs.* SHE), indicating the potential of KIBs to exhibit high operation voltage and energy density [12]. Compared to those of solvated Na^+ and Li^+ cations, the smaller size and lower activation energies of desolvation of solvated K^+ ions facilitate rapid ion transport through the electrode, significantly enhancing the rate performances of KIBs [13]. Moreover, KIBs employ the same "rocking chair" working mechanism as those of LIBs, where the K-ions shuttle between the cathode and anode to generate energy [14]. This similarity in their working mechanism may render KIBs more commercially viable than other battery technologies that require more complex or high-cost manufacturing processes.

The cathode is one of the most critical components of KIBs because it determines the energy density, cycle life, and safety of the battery [15]. However, due to the large ionic radius of K^+ compared to that of Li^+, the cathode materials of KIBs generally undergo several structural deteriorations during charging and discharging, resulting in capacity loss [16]. Therefore, identifying the proper cathode to enable stable K^+ storage is necessary. Various cathode materials for KIBs, including layered oxides, polyanion compounds, and Prussian blue analogs, have been investigated. Among them, layered transition metal (TM) oxides (K_xTMO_2; $0 < x \leq 1$, TM = Mn, Co, Cr, V) have been extensively studied due to their high theoretical capacities, simple synthetic processes, and reasonable ion diffusivity [17–21]. In particular, Mn-based layered oxides (K_xMnO_2) have been extensively investigated, but they face challenges such as rapid rate of capacity decay and limited power capability, primarily owing to their structural instability. The Jahn–Teller distortion of Mn^{3+} in Mn-based layered oxides is the main problem causing the poor cycling performance. Mn within cathode materials generally exists in a mixed-valence state of Mn^{3+} and Mn^{4+}. In the layered oxides, Mn^{4+} forms undistorted $[MnO_6]$ octahedra, thereby establishing stable crystal structures, but the presence of high-spin Mn^{3+}, with an electron configuration of ($t_{2g}^3 e_g^1$) in its 3d orbital, induces Jahn–Teller distortion. The lone electron in the e_g orbital can occupy the d_{z^2} or $d_{x^2-y^2}$ orbital, leading to the asymmetric elongation or compression of the octahedral structure [22]. These geometric distortions with longer Mn–O axial bonds generally reduce the structural stability due to the asymmetric

changes in the Mn–O bond lengths of the $[MnO_6]$ octahedra during charge-discharge process, resulting in structural strain with anisotropic volume changes. In addition, the dissolution of Mn^{2+} into the electrolyte leads to a decrease in the voltage and capacity of the battery [23].

Alongside the structural degradation caused by the Jahn–Teller distortion, the multiple phase transitions during cycling also contribute to the internal structural instability [24]. For example, K^+/vacancy ordering caused the complex phase transition, which is the main problem that degrades the electrochemical performances of Mn-based layered oxide cathodes [25]. When K ions are extracted from the structure during charging, the repulsive forces between O^{2-} and O^{2-} ions significantly increase. To prevent the breakdown of the TM–O bonds, therefore, the layered oxide structure in the TM layer glides in an interplanar direction, leading to multiple phase transitions [26]. Ceder et al. [17] reported that P3-$K_{0.5}MnO_2$ undergoes complex phase transitions such as P3–O3–X (unknown phase), imposing a substantial strain on the structure and resulting in the gradual degradation of the electrochemical performance. To overcome the structural instability of layered potassium manganese oxide, many works in enhancing the electrochemical performance through the optimization of the composition via doping with various active and/or inactive metals has been introduced [27–35].

Mg and Cu are promising candidates because of their similar ionic radii. Mg^{2+} (0.72 Å) and Cu^{2+} (0.73 Å) are suitable substitutes for Mn^{3+} (0.64 Å) within the TMO_2 slab, causing no significant change in the crystal structure [36]. Introducing low oxidation state of Mg^{2+} and/or Cu^{2+} stabilizes the crystal structure with the substitution of Mn^{3+}, which can increase the average oxidation state of Mn to Mn^{4+}; this results in the strong TM–O bonding interactions, eventually reducing the Jahn-Teller stress effect of Mn-based layered oxide cathodes. Recently, the effects of Mg and/or Cu substitution within layered manganese oxide cathodes have been reported [27,31,37,38]. However, the fundamental understandings of how the Mg and Cu co-substitution can improve the electrochemical K^+ storage properties of Mn-based layered oxide cathodes by suppressing the Jahn–Teller distortion of Mn^{3+} is still unclear.

In this study, we systematically investigated the effect of the Mg and Cu co-substitution in the P3-$K_{0.5}Mn_{0.8}Mg_{0.1}Cu_{0.1}O_2$ (P3-KMMCO) cathode by comparing with Mg and Cu mono-substituted cathodes. The presence of Mg and Cu within the TMO_2 slab plays the critical functions to enhance the electrochemical properties of the P3-$K_{0.5}Mn_{0.8}Mg_{0.1}Cu_{0.1}O_2$ cathode: 1) mitigating the Jahn-Teller stress effect by regulating the oxidation state of Mn to $Mn^{3.875+}$; 2) improving the structural stability by enhancing the TM–O bonding strength; 3) enabling the fast K^+ diffusion kinetics by enlarging the K interslab distance. In details, incorporating Mg^{2+} effectively mitigates K^+/vacancy ordering, increasing the cyclic performance [27,39,40] while Cu^{2+}, with its half-filled e_g orbital, increases electron delocalization, thereby improving the power capability [31]. As a result, the P3-KMMCO cathode demonstrates the excellent cycle retention and power capability with reversible phase transition of P3–O3 during charge-discharge process [17]. Theoretical and experimental studies were combined to unravel the relationship between structural and electrochemical properties of the P3-KMMCO cathode during charge-discharge process.

2. Results and discussion

2.1. Synthesis and characterizations

The $K_{0.5}MnO_2$, $K_{0.5}Mn_{0.9}Mg_{0.1}O_2$, $K_{0.5}Mn_{0.9}Cu_{0.1}O_2$, and $K_{0.5}Mn_{0.8}Mg_{0.1}Cu_{0.1}O_2$ cathodes were synthesized using typical solid-state reactions. ICP-OES analysis indicates that the stoichiometric atomic ratios of the elements within each sample match those designed (Table S1). The Rietveld refinement data determined using the X-ray diffraction (XRD) patterns reveal that the samples are crystallized well into P3-type layered structures with *R3m* symmetries, regardless of mono- or co-substitution (Fig. 1a and 1b and Fig. S1). Hereafter, the $K_{0.5}MnO_2$, $K_{0.5}Mn_{0.9}Mg_{0.1}O_2$, $K_{0.5}Mn_{0.9}Cu_{0.1}O_2$, and $K_{0.5}Mn_{0.8}Mg_{0.1}Cu_{0.1}O_2$ samples are denoted P3-KMO, P3-KMMO, P3-KMCO, and P3-KMMCO, respectively. When 0.2 mol of Mn is replaced by Mg or Cu via mono-substitution, peaks representing impurity phases, such as MgO or CuO, are observed in the XRD patterns (Fig. S2). Remarkably, however, Mg and Cu are successfully incorporated into the P3-KMO crystal even after replacing 0.2 mol of Mn. This is because co-substitution with Mg and Cu increases the entropy within the TMO_2 slab and thus decreases the formation energy, thereby leading to the formation of the P3 phase without impurities [41,42]. The detailed structural properties of P3-KMO, P3-KMMO, P3-KMCO, and P3-KMMCO are summarized in **Table S2**. As shown in Table S2 and Fig. S3, incorporating Mg and/or Cu into the structure leads to shifts in the (003) planes of P3-KMMO, P3-KMCO, and P3-KMMCO to higher angles, indicating decreases in *c*. This can be explained based on the concept of cation potential, which easily explicates the interslab distances of transition metal (TM) and alkali metal (AM) slabs [43]. The ionic potential, which is determined by the ionic radii and charges of the cations, is a factor in determining the bonding strength between the TM and O ions. It reflects the cation polarization power, which can be defined as $\Sigma w_i n_i / R_i$, where w_i represents the content of TM ions with charge number n and radius R. A higher cationic potential indicates higher charge densities at the surfaces of the TM ions, resulting in more covalent TM–O bonds. The co-substitution with Mg^{2+} and Cu^{2+} introduces more Mn^{4+}, which exhibits a higher oxidation state and smaller ionic radius than those of Mn^{3+} (0.64 Å for Mn^{3+}, 0.53 Å for Mn^{4+}), increasing the cationic potential. Therefore, the ionic potential increases with substitution of divalent metal ions, such as Mg^{2+} and Cu^{2+}, enhancing the bonding strength between the TM and O ions while weakening that between K and O. This leads to a decrease in the TMO_2 slab distance and an increase in the KO_2 slab distance [44]. Fig. 1c illustrates the slab distance change upon the Mg and Cu

co-substitution. As shown in Table S3, P3-KMMCO displays the lowest TMO_2 slab spacing and highest KO_2 interslab distance compared to those of the other samples. Moreover, by introducing two foreign metals (Mg and Cu) with different ionic radii and chemical properties compared to those of Mn, the degree of disorder within the TMO_2 slab increases, resulting in a higher thermodynamic stability than those of other samples [45,46]. The enhanced structural stability of the TMO_2 slab with an increased degree of disorder and a large KO_2 interslab distance can supports the suppression of the structural stress of P3-KMMCO during electrochemical K^+ de/intercalation. Scanning electron microscopy (SEM) reveals that all samples exhibit plate-shaped particle morphologies, with particle sizes ranging from 1 to 3 μm, regardless of chemical composition, suggesting that mono- and co-substitution do not significantly affect the particle sizes and shapes of the samples (Fig. S4). To obtain more information about the crystal structure, high-resolution transmission electron microscopy (HR-TEM) analysis was performed. Figs. S5a and 5b shows that the interplanar distances of 0.70 nm and 0.69 nm correspond to the (003) crystal planes of P3-KMO and P3-KMMCO cathodes, respectively, which is consistent with the result from Rietveld refinement (Table S2). Additionally, transmission electron microscopy with energy dispersive X-ray analysis (TEM-EDS) confirms the uniform distributions of K, Mn, Mg, and Cu within P3-KMMCO (Fig. 1d). To study the average valence states of P3-$K_{0.5}MnO_2$ (P3-KMO) and P3-$K_{0.5}Mn_{0.8}Mg_{0.1}Cu_{0.1}O_2$ (P3-KMMCO), we conducted XPS analysis. The Mn 2p spectra can be divided into two sets: the peaks located at 641.9 eV and 653.3 eV are related to Mn^{3+}, while the signals centered at 643.2 eV and 654.6 eV are attributed to Mn^{4+} (Figs. S6a and 6b) [47]. In P3-KMO, the average oxidation state of Mn is 3.5^+. After the partial substitution of Mg^{2+} and Cu^{2+} at the Mn site in P3-KMO, the average Mn oxidation state increases from 3.5^+ to 3.875^+ (Fig. S6c). The measured results are consistent with the calculation of the charge compensation mechanism; the introduction of divalent Mg^{2+} and Cu^{2+} increase the average Mn valence state in P3-KMMCO. This result indicates that the Mn average valence state is regulated by the introduction of Mg and Cu in the P3-KMO cathode.

2.2. Electrochemical properties

Electrochemical measurements were conducted to validate the stabilization of the crystal structure by regulating the oxidation state of Mn via co-substitution with Mg and Cu. The electrochemical performances of the prepared cathodes were evaluated in half cells with K metal as their anodes in the voltage range of 1.5–3.9 V. Fig. 2a and 2b
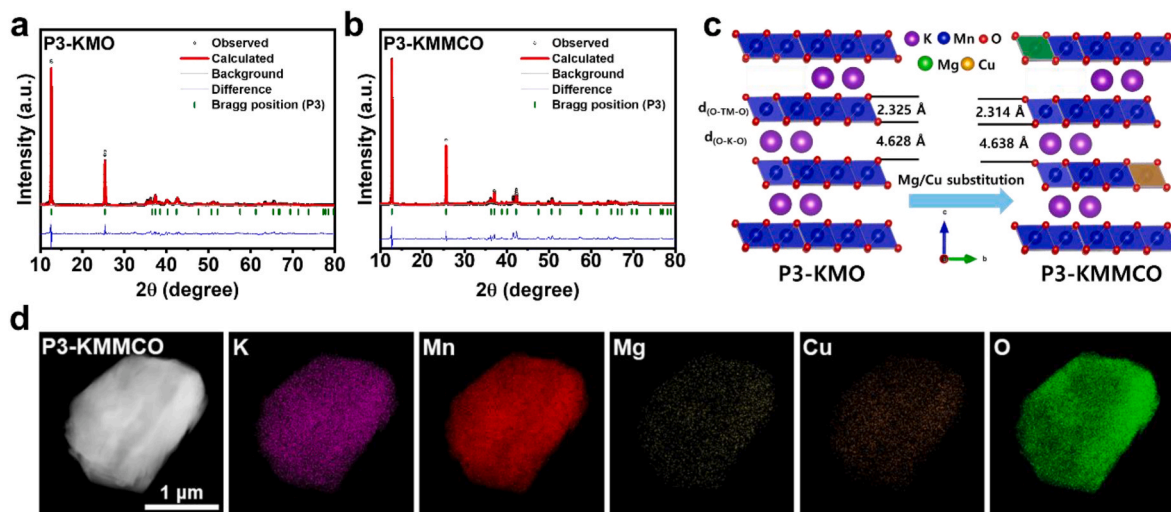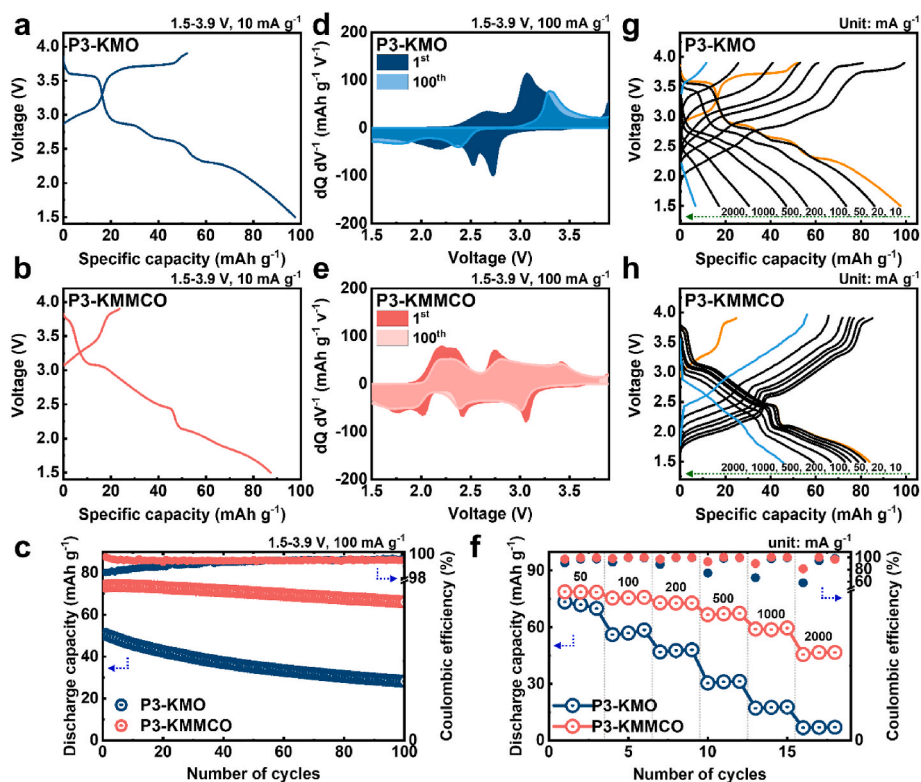

Fig. 1. Rietveld refinement of the XRD patterns of (a) P3-KMO and (b) P3-KMMCO cathodes. (c) Schematic of the crystal structure of the P3-KMMCO cathode. (d) TEM-EDS mapping images of the P3-KMMCO cathode.

Fig. 2. Galvanostatic charge-discharge curves of the 1st cycle of (a) P3-KMO and (b) P3-KMMCO cathodes at 10 mA g^{-1} in the voltage range 1.5–3.9 V. (c) Cycling performances of P3-KMO and P3-KMMCO at 100 mA g^{-1}. Differential capacity curves of the (d) P3-KMO and (e) P3-KMMCO cathodes. (f) Rate capabilities of P3-KMO and P3-KMMCO cathodes at various current densities from 50 to 2000 mA g^{-1}. Galvanostatic charge-discharge curves of (g) P3-KMO and (h) P3-KMMCO cathodes at various current densities.

respectively show the 1st charge-discharge voltage profiles of the P3-KMO and P3-KMMCO cathodes at a current density of 10 mA g^{-1}. Fig. S7 shows the 1st charge-discharge voltage profiles of the P3-KMMO and P3-KMCO cathodes, respectively. The charge-discharge curves of the P3-KMO cathode display several voltage plateaus and steps, which reflect the multi-stage phase transformation occurring along with the gliding of the TMO$_2$ slab [48]. Upon substitution at the Mn sites using 10 mol.% Mg or Cu, the P3-KMMO and P3-KMCO cathodes exhibit less voltage steps than that of the P3-KMO cathode. Notably, the P3-KMMCO cathode produces very smooth charge-discharge curves, indicating that co-substitution with 10 mol.% Mg and Cu effectively suppresses the K$^+$/vacancy ordering and gliding of the TMO$_2$ slab. Although substitution with electrochemically inactive Mg and/or Cu decreases the 1st discharge capacity (P3-KMO: 97.5 mAh g^{-1}, P3-KMMO: 95.6 mAh g^{-1}, P3-KMCO: 92.1 mAh g^{-1}, P3-KMMCO: 87.2 mAh g^{-1}), the cycling stability can be significantly enhanced (Fig. 2c, Figs. S8 and S9). Notably, the P3-KMMCO cathode displays an outstanding capacity retention of 90.1% compared to those of the other cathodes (P3-KMO: 59.8%, P3-KMMO: 63.1%, and P3-KMCO: 51.2%) at 100 mA g^{-1} after 100 cycles. The differential capacity (dQ dV^{-1}) analysis shown in Fig. 2d and 2e and Fig. S10 reflects the different cycling behaviors of the P3-KMO and P3-KMMCO cathodes, because the peak intensities and positions of each electrode material reflect the reversibility of the redox processes. Furthermore, observing the sharpness and positions of the peak aids in understanding reaction kinetics and overall polarization—including ohmic, activation, and concentration polarizations [49]. By analyzing the intensity and peak positions during cycles, the extent of capacity loss and changes in polarization can be evaluated. Upon multiple cycling, the redox peaks of the P3-KMMCO cathode remain very stable and thus indicate better reversible K$^+$ de/intercalation than P3-KMO cathode, signifying the effective suppression of the K$^+$/vacancy ordering and gliding of the TMO$_2$ slab (Fig. 2e and Fig. S10b). However, the redox

peaks of the P3-KMO cathode with large voltage polarizations are no longer observed after the 100th cycle (Fig. 2d and Fig. S10a). To further highlight the effectiveness of co-substitution with Mg and Cu in stabilizing the crystal structure of the P3-KMMCO cathode, we compared the electrochemical properties to those of the P3-KMO cathode within the extended voltage range of 1.5–4.2 V (Fig. S11 and Fig. S12). The high voltage study highlights the excellent electrochemical performance of the P3-KMMCO cathode in K-cell. Remarkably, the P3-KMMCO cathode exhibits remarkable improvements in electrochemical performance, demonstrating a superior capacity retention of 77.6% after 100 cycles at 100 mA g^{-1} (Fig. S13). A new prominent oxidation peak is observed at approximately 4.1 V accompanied by the complete disappearance of the corresponding reduction peak in the dQ dV^{-1} curve of the P3-KMO cathode (Fig. S14), which may be associated with the irreversible phase transition occurring at high-voltage region over 3.9 V. In addition, the P3-KMO cathode undergoes irreversible structural changes at high-voltage region during K$^+$ de/intercalation, resulting in severe capacity fading (Fig. S15a). In contrast, co-substitution with Mg and Cu results in an enhanced reversible redox reaction in the dQ dV^{-1} analysis, even in the extended voltage range of 1.5–4.2 V, supporting the noticeable enhancement in the cycling stability (Fig. S15b). Furthermore, the synergetic effect of Mg and Cu co-substitution enhances the reversibility of the K$^+$ insertion/extraction reaction and diffusion kinetics. Power capability studies at various current densities (50–2000 mA g^{-1}) clearly confirm the superior performance of the P3-KMMCO cathode compared to those of the P3-KMO, P3-KMCO, and P3-KMMO cathodes (Fig. 2f–h, Fig. S16, and Fig. S17). The P3-KMMO cathode exhibits improved performances at relatively low rates, indicating that Mg effectively stabilizes the structure, leading to a higher reversible capacity than P3-KMCO. Additionally, P3-KMCO demonstrates better power capability at rates above 200 mA g^{-1} compared to P3-KMMO. The hybrid orbitals of Cu and O, owing to the electronic configuration of

Cu^{2+} with its half-filled e_g orbital, increase electron delocalization, thereby improving the kinetics. The combination scenario of these individual effects significantly enhances the kinetics and thermal dynamic stabilities; as a result, the P3-KMMCO cathode delivered 50% of its initial capacity at 10 mA g^{-1}, even at extremely high current density of 2000 mA g^{-1} in comparison with only 7% for the P3-KMO cathode. Notably, P3-KMMCO demonstrate the superior capacity retention of 81.4 % after 100 cycles at 500 mA g^{-1}. (Fig. S18). The enhanced electrochemical performance indicates that co-substitution with Mg and Cu displays positive effects in terms of stabilizing the crystal structure and increasing the K$^+$ kinetics during K$^+$ de/intercalation.

To gain a better understanding of the enhanced K$^+$ kinetics, galvanostatic intermittent titration technique (GITT) and cyclic voltammetry (CV) measurements were conducted for P3-KMO and P3-KMMCO cathodes. The K$^+$ diffusion coefficient (D_{K^+}) was determined using GITT during initial cycle and calculated according to the following equation [50]:

$$D_{K^+} = \frac{4}{\pi\tau}\left(\frac{n_m V_m}{S}\right)^2 \left(\frac{\Delta E_S}{\Delta E_t}\right)^2$$

where τ is the duration of current pulse (s); n_m is the number of moles (mol); V_m is the molar volume of the cathode (cm^3 mol^{-1}); S is the area of the cathode (cm^2); ΔE_s is the voltage change in steady-state; and ΔE_t is the voltage change during the constant current pulse, excluding the iR drop. The diffusion coefficients of K$^+$ (D_{K^+}) for the P3-KMO and P3-KMMCO cathodes were calculated during charging and discharging during the first two cycles. The calculated D_{K^+} show that the P3-KMMCO cathode exhibits a higher ion diffusivity, ranging from 5.01×10^{-9} to 4.26×10^{-12} cm^2 s^{-1} with average compared to the P3-KMO cathode, which ranges from 1.32×10^{-9} to 6.76×10^{-11} cm^2 s^{-1} as in the first cycle (Figs. S19a and 19b). Notably, the D_{K^+} value of P3-KMO cathode at the end of charge was only one-sixtieth that of the P3-KMMCO cathode, indicating that the unfavorable phase transition in the high-voltage region led to sluggish K$^+$ kinetics. Furthermore, in the second cycle, P3-KMO exhibits notable fluctuations, while P3-KMMCO demonstrates stable behavior (Figs. S19c and 19d). This result suggest that the Mg and Cu substitution effectively suppressed irreversible phase transition in the high volte region, enhancing the structural stability with K$^+$ ion kinetics, resulting in superior rate capabilities.

The CV analysis of P3-KMO and P3-KMMCO cathodes was conducted at various scan rate from 0.1 to 1.0 mV s^{-1} in the voltage region of 1.5–3.9 V. The CV profiles reveal distinct pair of oxidation and reduction peaks. As shown in Figs. S20a and 20b, both the peak currents and overpotentials increase with the rising in scan rate. Notably, for the P3-KMO cathode, the pairs of redox peaks gradually merge as the scan rate increases, while the peak configuration of the P3-KMMCO cathode was largely maintained, suggesting that the voltage polarization for the KMMCO cathode is significantly lower than that of P3-KMO cathode. The electrochemical diffusion (faradic) and non-diffusion (non-faradic) kinetic behaviors of P3-KMO and P3-KMMCO cathodes were calculated and compared using the following equation:

$$i = av^b$$

where i and v are the peak current (mA) and related scan rate (mV s^{-1}), respectively, and a and b are variables. For example, the calculated b values describe the storage process [51]; if the value is 0.5, then it is exclusively a diffusion-controlled process; if the value is 1.0, it implies a capacity-controlled process. Based on the relationship between log (i)-log(V) for different redox peak, the notable slope b values are 0.55 and 0.515 for P3-KMO and P3-KMMCO cathodes, respectively (Fig. S20c). In addition, the contributions of diffusion-controlled and capacitive-controlled processes to K$^+$ storage were quantitatively measured using the following equation:

$$i(V) = k_1 v + k_2 v^{1/2}$$

The first and second terms represent the capacitive- and diffusion-controlled redox reactions, respectively [52]. Based on this, the capacitive- and diffusion-controlled contributions for both cathodes were calculated (Figs. S20d and 20e). The overall diffusion contribution of P3-KMMCO were higher than those of P3-KMO at scan rates ranging from 0.1 mV s^{-1} to 1 mV s^{-1}. These results suggest that the reduced voltage polarization, achieved through enhanced structural stability and faster K ion kinetics through the Mg and Cu co-substitution strategy, contributes to improved performance.

2.3. Charge compensation mechanism

Synchrotron-based *ex situ* X-ray absorption near-edge structure (XANES) spectroscopy was used to examine the oxidation states of the Mn and/or Cu atoms within the P3-KMO and P3-KMMCO cathodes during their electrochemical reactions. Fig. S21 shows a comparison of the Mn K-edge XANES spectra of the pristine (before cycling) and 1st discharged, and 2nd charged states. Mn_2O_3 (Mn^{3+}) and MnO_2 (Mn^{4+}) were used as reference samples to confirm the change in the Mn oxidation state [48]. In the pristine state, the average oxidation state of Mn within the P3-KMO cathode is an intermediate value between Mn^{3+} and Mn^{4+} (Fig. S21a), whereas the Mn K-edge of the P3-KMMCO cathode shifts to a higher energy level. The energy level of Mn within the P3-KMMCO cathode is close to the $Mn^{(4+)}O_2$ reference energy region, indicating that the Mn oxidation state increases after co-substitution with Mg^{2+} and Cu^{2+} (Fig. S21b). In the 1st discharged state, the Mn K-edges of the P3-KMO and P3-KMMCO cathodes shift to lower energy levels, indicating decreases in the oxidation of their Mn species owing to K$^+$ intercalation within their crystal structures. After the 2nd charge to 3.9 V, the oxidation states of the Mn ions within both cathodes are close to that of Mn^{4+}, indicating their reversible Mn^{3+}/Mn^{4+} redox reactions. To further verify the possibility of the Cu^{2+}/Cu^{3+} redox reaction, the Cu K-edge of the P3-KMMCO cathode was measured (Fig. S21c). The oxidation state of Cu within the KMMCO cathode in the pristine state is close to the $Cu^{(2+)}O$ reference energy region. No changes are observed in the oxidation state of Cu within the P3-KMMCO cathode in the 1st discharged and 2nd charged states. Additionally, to further investigate the possibility of the $Cu^{2+/3+}$ redox reaction for the P3-KMMCO, we conducted *ex situ* XPS analysis. Fig. S22 shows the Cu 2p XPS spectra for the pristine cathode before the electrochemical reaction initiation with those for the 1st charged and discharged samples, respectively. The Cu $2p_{1/2}$ and $2p_{3/2}$ spectra of the samples are assigned at ~953 eV and ~932 eV with Cu^{2+} satellite peaks, indicating that Cu exists Cu^{2+} oxidation state in the P3-KMMCO [53]. After the charge and discharge process of the P3-KMMCO cathode material, no significant change in binding energy is observed. All the results reveals that the Cu remains electrochemically inactive in the P3-KMMCO cathode during the charge and discharge process, which is well consistent with the XANES result (Fig. S21c). XANES spectroscopy and ex situ XPS analysis reveals that the Mn ions are only involved in the redox reactions of the P3-KMO and P3-KMMCO cathodes, whereas Cu remains electrochemically inactive in the P3-KMMCO cathode [54].

2.4. Structural evolution

Synchrotron in situ XRD was performed to validate the structural evolution of the P3-KMO and P3-KMMCO cathodes in the voltage range of 1.5–3.9 V at 10 mA g^{-1}. The peak intensities of the XRD patterns are shown as contour plots in Fig. 3a and 3b, along with the galvanostatic charge-discharge curves during the first two cycles. During the charging of both cathodes, the (003) and (006) peaks shift to lower angles due to the increased electrostatic repulsion between the O^{2-} ions upon K$^+$ deintercalation, whereas the (101) and (102) peaks shift to higher angles due to the decrease in the ionic radius of Mn^{3+} upon conversion to Mn^{4+} [55]. As the increases to 3.7 V, the (101), (012), and (015) peaks of the P3 phase decrease in intensity, accompanied by the emergence of a new
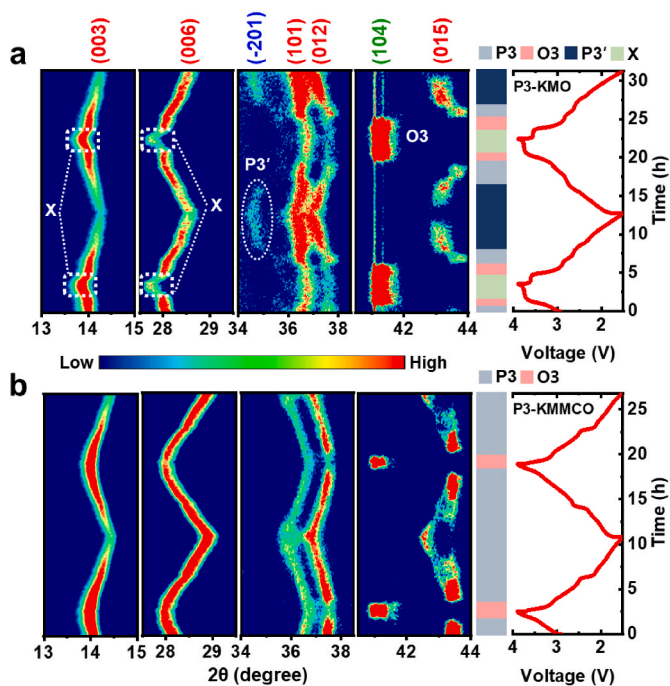
Fig. 3. Contour plots of the in situ XRD data and charge-discharge curves of the first two cycles of charge and discharge at 20 mA g^{-1} in the voltage range of 1.5–3.9 V, as obtained via in situ XRD of (a) P3-KMO and (b) P3-KMMCO cathodes.

peak at $2\theta = 41°$, which corresponds to the (104) peak of the O3-type structure. This phase transition from P3 to O3 is mainly due to the gliding of the TMO$_2$ slab to inhibit the cleavage of the TM–O bonds, with the K ions located at the edge-shared octahedral sites with ABCABC oxygen packing. Upon further charging to 3.8 V, the (003) and (006) peaks of the P3-KMMCO cathode exhibit consecutive motions (Fig. 3b). In contrast, the P3-KMO cathode undergoes a discontinuous phase transition, where new peaks associated with the "X" phase emerge at low angles, with the sudden shift of the (003) and (006) peaks of the P3 phase (Fig. 3a). Similar to our result, Ceder et al. [17] reported an "X" phase within the P3-K$_{0.5}$MnO$_2$ cathode at 3.9 V, where the "X" phase indicates rapid, violent structural changes, with sudden variations in the peak positions. During discharging, the P3-KMMCO cathode exhibits a reversible phase transition, such as O3 to P3, demonstrating the excellent structural reversibility of the cathode. In contrast, the P3-KMO cathode undergoes complex phase transitions, such as X–O3–P3–P3′, during discharging. K$^+$ intercalation into the crystal structure at the end of discharge, in particular, leads to the monoclinic P3′ phase, which is characterized by the appearance of the (−201) peak at 34.5°. This activates the Jahn–Teller stress effect of the structure, resulting in the distortion of the regular diamond of the a-b plane into a rectangle with different a and b values. Eventually, these complex phase transitions decrease reversible K$^+$ de/intercalation, leading to the rapid capacity fading of the P3-KMO cathode [48]. In situ XRD clearly shows that co-substitution with Mg and Cu can enhance the TM–O bonding strength and thus effectively suppress complex, irreversible phase transitions by regulating the Jahn–Teller-active Mn^{3+}.

2.5. Computational insights

The theoretical properties of K$_x$[Mn$_{0.8}$Mg$_{0.1}$Cu$_{0.1}$]O$_2$ during K$^+$ de/intercalation were investigated using first-principles calculations based on structural information obtained from Rietveld refinement. Various K$^+$/vacancy configurations within P3- and O3-K$_x$[Mn$_{0.8}$Mg$_{0.1}$Cu$_{0.1}$]O$_2$ ($0 \leq x \leq 1$) were plotted in the form of a convex-hull plot. The theoretical redox potentials are obtained from the lowest formation of each composition and the following equation:

$$V = -\frac{E\left[K_{x_2}\left[Mn_{0.8}Mg_{0.1}Cu_{0.1}\right]O_2\right] - E\left[K_{x_1}\left[Mn_{0.8}Mg_{0.1}Cu_{0.1}\right]O_2\right] - (x_2 - x_1)E[K]}{(x_2 - x_1)F}$$

Where V is the average redox potential in the compositional range of K$_x$[Mn$_{0.8}$Mg$_{0.1}$Cu$_{0.1}$]O$_2$ ($x_1 < x < x_2$), and $E\left[K_x\left[Mn_{0.8}Mg_{0.1}Cu_{0.1}\right]O_2\right]$ is the most stable formation energy each K$_x$[Mn$_{0.8}$Mg$_{0.1}$Cu$_{0.1}$]O$_2$ configuration. F and $E[K]$ represent the Faraday constant and formation energy of K metal, respectively. As shown in Fig. 4a, more than 0.5 mol of K$^+$ ions can be reversibly extracted from/inserted into the P3-KMMCO structure within the available voltage range. Furthermore, the calculation results suggest that the O3-phase in P3-KMMCO is thermodynamically more stable than the P3-phase when the K content in the structure decreases or below 0.25 mol. However, charging to a high voltage beyond the available range is required for K$^+$ extraction from K$_{0.25}$[Mn$_{0.8}$Mg$_{0.1}$Cu$_{0.1}$]O$_2$, suggesting that full K$^+$ deintercalation from P3-KMMCO during charging for KIBs is challenging. Moreover, comparing the theoretically predicted redox potentials of P3-KMMCO and experimentally measured charge/discharge profile (Fig. 4b) indicates a good match. Fig. 4d shows the calculated structural changes within P3-KMMCO during K$^+$ de/intercalation. As the K content within the structure decreases from 1 to 0.25 mol, the c-lattice parameter gradually increases from 18.305 to 19.112 Å, which is attributed to the O^{2-}-O^{2-} repulsion [19]. Despite the phase transition from P3 to O3 occurring between a K content of 0.5 and 0.25 mol, the difference in the c lattice parameters c of the P3-K$_1$[Mn$_{0.8}$Mg$_{0.1}$Cu$_{0.1}$]O$_2$ and O3-K$_{0.25}$[Mn$_{0.8}$Mg$_{0.1}$Cu$_{0.1}$]O$_2$ phases is only ~4.2%. These calculated results indicate that P3-KMMCO can deliver a stable cycle performance owing to the small structural change during K$^+$ de/intercalation (Fig. 2c). Moreover, as depicted in Fig. 4c, the predicted changes in the c lattice parameter, reflecting the P3-O3 phase transition during charging, closely match the results of operando XRD, where the (003) peak shifts to lower 2θ angles.

To verify the impact of Mg and Cu on the diffusion kinetics of K$^+$ within the structure, as illustrated in Fig. 5a, we used the nudged elastic band (NEB) method to establish the theoretical activation energy barriers necessary for K$^+$ diffusion within P3-KMO and P3-KMMCO [19,56]. As shown in Fig. 5b and 5c, the required activation barrier energies of P3-KMO and P3-KMMCO are ~642.03 and ~521.78 meV, respectively. These results suggest that P3-KMMCO facilitates K$^+$ diffusion more effectively near the MgO$_6$ and CuO$_6$ octahedra compared to P3-KMO, which is attributed to the suppressed Jahn–Teller distortion of Mn^{3+} via simultaneous substitution with Mg and Cu within the structure. Furthermore, to confirm the enhanced rate performance of P3-KMMCO compared to that of P3-KMO, we compared the bandgap (E$_g$) energies, which indicate the electronic conductivity of the materials. As shown in Fig. 5d and 5e, density of states (DOS) calculations were performed, using the HSE06 hybrid functional in first-principles calculations. The bandgap (E$_g$) energies of P3-KMO and P3-KMMCO are ~0.85 and ~0.43 eV, respectively, which suggests that P3-KMMCO displays an improved electronic conduction compared to that of P3-KMO. In addition, the delocalized electrons of Cu^{2+} within P3-KMMCO suggest the potential for faster charge transport, thereby enhancing the kinetics. Moreover, the hybridization of the Cu^{2+} 3d and O 2p electron spins forms strong Cu–O covalent bonds, which reduce the thicknesses of the TMO$_2$ slabs, resulting in an improved structural stability and enhanced kinetic properties [57]. Thus, the predicted calculation results of the NEB and DOS analyses indicate that co-substitution with Mg and Cu within the structure can result in the more enhanced power capability of P3-KMMCO for KIBs.

Furthermore, first-principles calculations confirmed that simultaneous substitution with Mg and Cu successfully suppresses the local structural changes caused by Jahn–Teller distortion due to Mn^{3+}. This
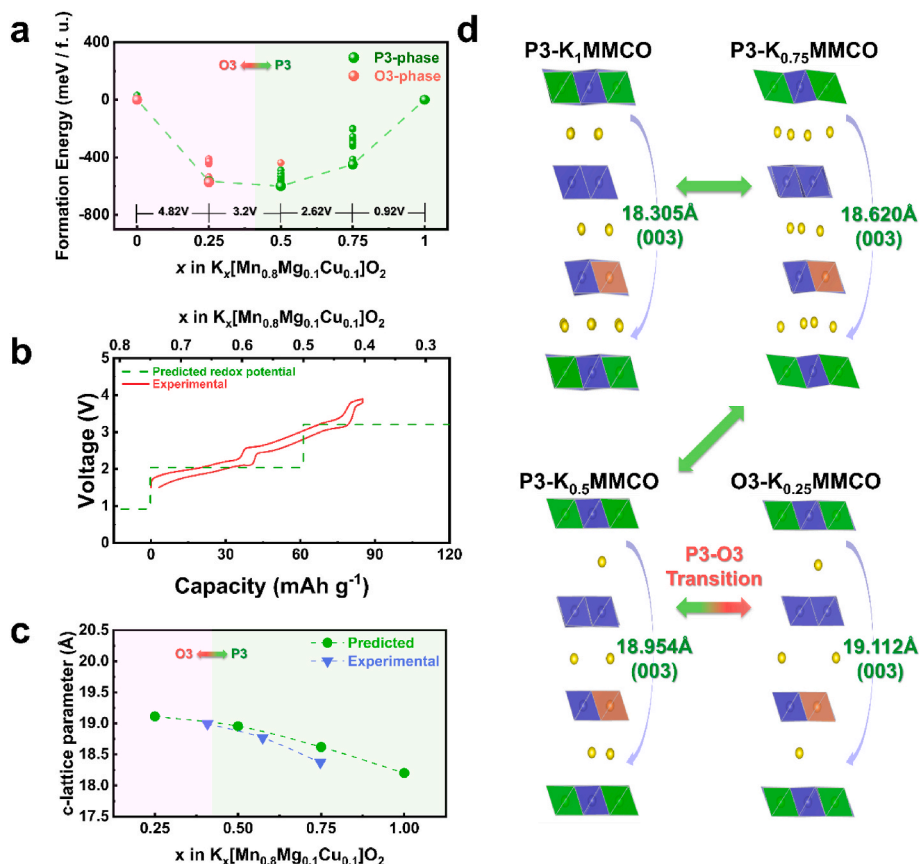
Fig. 4. (a) Convex-hull plot of various P3-/O3-$K_x[Mn_{0.8}Mg_{0.1}Cu_{0.1}]O_2$ configurations ($0 \leq x \leq 1$) with theoretical redox potentials. (b) Comparison of the experimental charge-discharge curves and voltage curves predicted using first-principles calculations. (c) Comparison of the c-lattice parameters of P3-/O3-$K_x[Mn_{0.8}Mg_{0.1}Cu_{0.1}]O_2$ gained by first-principles calculation with the experimental values. (d) Structural changes in P3-/O3-$K_x[Mn_{0.8}Mg_{0.1}Cu_{0.1}]O_2$ as a function of the K content ($0 \leq x \leq 1$), predicted using first-principle calculation.

suppression reduces the effects of the difference in the Jahn–Teller distortion of Mn^{3+} within P3-KMO and P3-KMMCO on the bonding interactions within the $[MnO_6]$ octahedra. As shown in Fig. 6a, the Mn–O bond lengths of P3-KMO vary considerably, with a difference of approximately 0.27 Å between the Mn–O_1 and Mn–O_2 bond lengths. In contrast, the Mn-O bond lengths of P3-KMMCO are relatively similar because of the suppression of the Jahn–Teller distortion of Mn^{3+}. Fig. 6b and 6c show plots of all predicted Mn–O bond lengths of P3-KMO and P3-KMMCO, as determined using DFT calculations, as bond populations for easy visualization. In the P3-KMMCO structure, the average Mn–O bond length ranges from 1.9 to 2.0 Å, displaying a narrower distribution than that of the P3-KMO structure, indicating the suppression of the Jahn–Teller distortion of Mn^{3+}. Therefore, these results indicate that the simultaneous substitution with Mg^{2+} and Cu^{2+} strengthens the TMO_2 slab, suppressing the irreversible phase transitions and enhancing structural stability, thereby leading to the superior electrochemical performance of P3-KMMCO compared to that of P3-KMO.

3. Conclusion

In summary, we propose the co-substitution with Mg and Cu to suppress the irreversible multiple phase transitions caused by the Jahn–Teller distortion of Mn^{3+}. The synergetic effect of Mg and Cu co-substitution effectively suppressed Jahn-Teller distortion, leading to an improved structural stability. As a result, the P3-KMMCO cathode exhibited an outstanding cycling stability, with a capacity retention of 90.1% after 100 cycles at 100 mA g^{-1}. Moreover, the P3-KMMCO cathode displayed a superior cycling stability with a higher charge cut-off voltage of 4.2 V, retaining 77.6% of its capacity at 100 mA g^{-1}.

Based on synchrotron in situ XRD, the P3-KMMCO cathode underwent reversible P3–O3 structural changes, and the multiple phase transitions upon K^+ de/insertion in the voltage range of 1.5–3.9 V were suppressed. Theoretical studies based on DFT calculations indicated that the enhanced structural stability and cycling performance could be ascribed to the suppressed Jahn–Teller distortion and rapid K-ion kinetics. We believe that the results demonstrated herein offer potential in enhancing the structural stabilities of the Mn-based layered oxides cathode for advanced KIBs.

4. Experimental section

4.1. Material synthesis

The P3-type $K_{0.5}Mn_{0.8}Mg_{0.1}Cu_{0.1}O_2$ (P3-KMMCO) was prepared using a simple solid-state reaction. For comparison, P3-type $K_{0.5}MnO_2$ (KMO), $K_{0.5}Mn_{0.8}Mn_{0.2}O_2$, $K_{0.5}Mn_{0.8}Cu_{0.2}O_2$, $K_{0.5}Mn_{0.9}Cu_{0.1}O_2$ (P3-KMCO), and $K_{0.5}Mn_{0.9}Mg_{0.1}O_2$ (P3-KMMO) were also synthesized using the same approach. The starting materials, including potassium carbonate (K_2CO_3, 99% Aldrich), manganese oxide (Mn_2O_3, 99% Aldrich), magnesium oxide (MgO, 99% Aldrich), and copper oxide (CuO, 99.9% Aldrich) were used in stoichiometric amounts. The precursor powders were mixed thoroughly and ground using an agate mortar. Subsequently, the final powders were prepared by annealing at 850 °C for 15 h in air at a heating rate of 5 °C/min. After cooling naturally to room temperature, the resulting samples were transferred into and stored in an Ar-filled glove box.
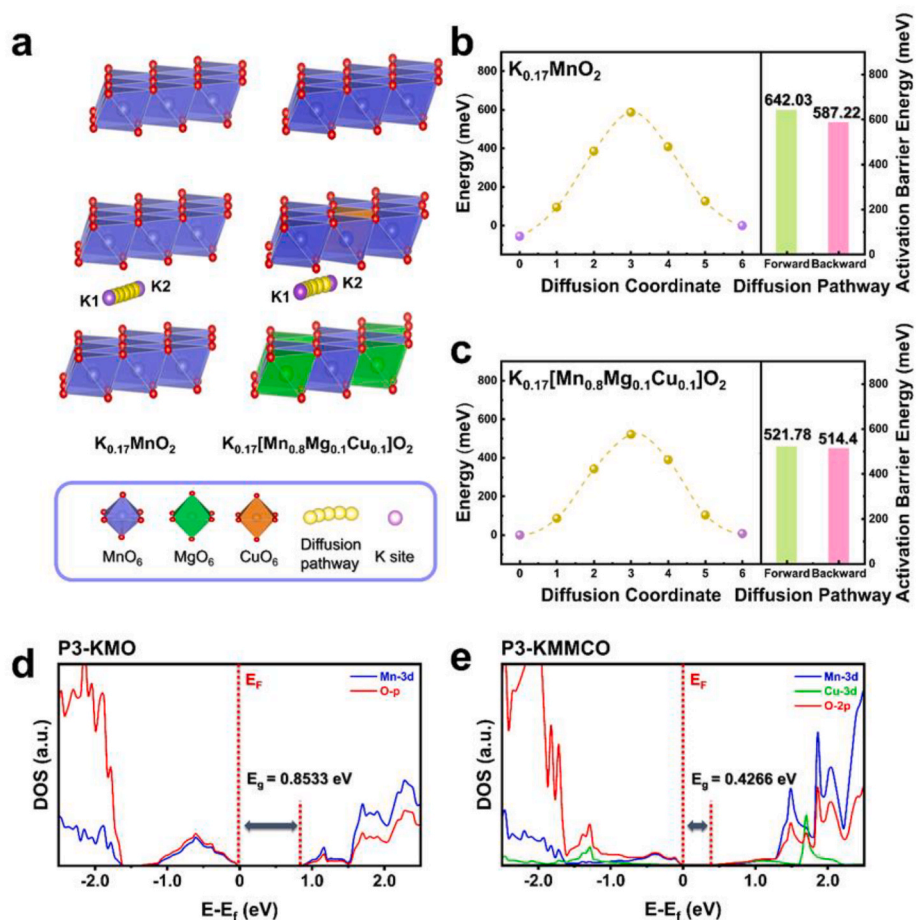
Fig. 5. (a) Predicted K$^+$ diffusion pathway in P3-K$_{0.17}$MnO$_2$ and P3-K$_{0.17}$[Mn$_{0.8}$Mg$_{0.1}$Cu$_{0.1}$]O$_2$. Predicted activation barrier energies of (b) P3-K$_{0.17}$MnO$_2$ and (c) P3-K$_{0.17}$[Mn$_{0.8}$Mg$_{0.1}$Cu$_{0.1}$]O$_2$ cathodes. Projected of states (pDOS) with band-gap of (d) P3-KMO and (e) P3-KMMCO cathodes.
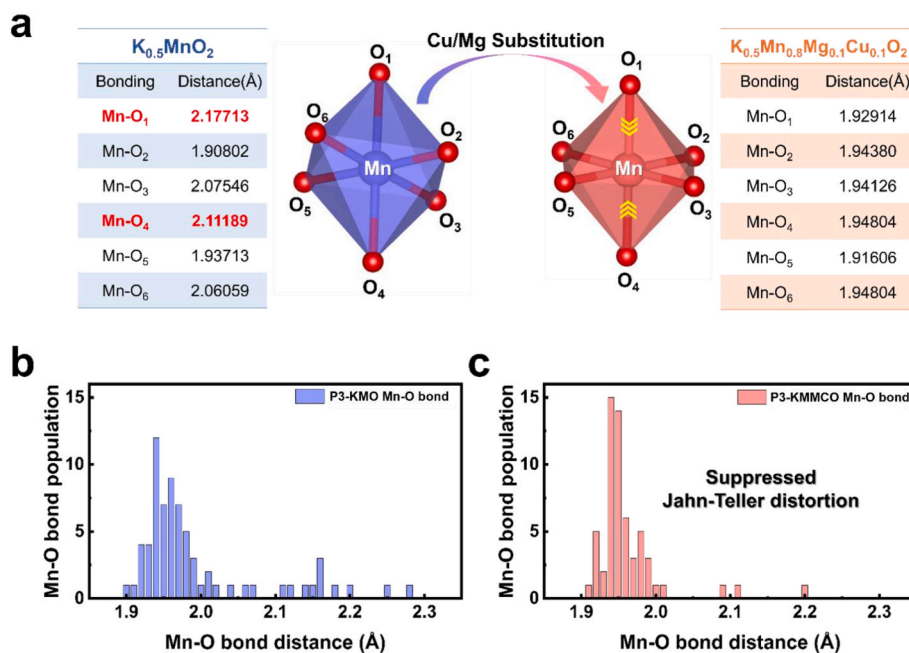

Fig. 6. (a) Comparison of the predicted Mn–O bond distances of [MnO$_6$] in P3-KMO and P3-KMMCO cathodes. through first-principles calculation. Mn–O bond population for comparison of predicted Mn–O bond distances of [MnO$_6$] in (b) P3-KMO and (c) P3-KMMCO cathodes.

4.2. Material characterization

The chemical compositions of the samples were confirmed via inductively coupled plasma-optical emission spectroscopy (ICP-OES) using an iCAP 7400 DUO (Thermo Fisher Scientific, Waltham, MA, USA). The crystal structures and morphologies of the prepared powders were identified via XRD using a diffractometer that employed Cu Kα radiation ($\lambda = 1.54178$ Å) over the 2θ range $10°$–$80°$. The raw XRD data were refined via the Rietveld process using the FullProf software (Institut Laue-Langevin, Grenoble, France), and the structural models derived from the refined data were constructed using the Visualization for Electronic Structural Analysis software (Tohoku University, Sendai, Japan). The microstructure of each sample was determined via scanning electron microscopy (SEM) using a Verios G4 UC (Thermo Fisher Scientific) and transmission electron microscopy (TEM) using a NEOARM (JEOL, Tokyo, Japan), whereas mapping was performed using energy-dispersive X-ray spectroscopy (EDS). X-ray photoelectron spectroscopy (XPS) using a PHI5600 (PerkinElmer, USA) measurements were performed. To investigate the structural evolution, the operando XRD patterns were utilized, with in situ XRD conducted using an Empyrean diffractometer (Malvern Panalytical, Malvern, UK) with Kα radiation. Synchrotron X-ray spectroscopy (XAS) was conducted at the BL7D beamline of the Pohang Light Source (Pohang, Republic of Korea). A high energy of 2.5 GeV and current of approximately 200 mA were employed to collect ex situ measurements of all recovered samples in their pristine, charged, and discharged states.

4.3. Electrochemical measurements

The working electrode used in the electrochemical tests was prepared by blending the active material, Super P (Alfar Aesar, USA), and poly(vinylidene fluoride) (Solvay, Belgium) at a weight ratio of 80:10:10 with *N*-methyl-pyrrolidone (NMP) using a mortar and pestle. The resulting slurry was coated onto an aluminum foil (Hoshen Corp., Japan) to a thickness of 200 μm using doctor blade and dried for 6 h at 110 °C in a vacuum oven. Subsequently, the dried electrode was roll pressed between stainless-steel twin rollers under a constant load of 3.5 kN and punched into circular discs (14 mm in diameter). The average loading mass of active materials on the electrode was 3.0–4.0 mg cm^{-2}. The assembled CR2032-type coin cell comprised the cathode electrodes and K metal anode electrodes (16 mm in diameter) separated by a glass fiber filter (Advantec, USA) in 0.5 M KPF$_6$ in ethylene carbonate/diethylene carbonate (EC/DEC = 1:1 in volume. Galvanostatic electrochemical charge-discharge were performed on half cells under a constant current density at 30 °C in the voltage range of 1.5–3.9 V, and 1.5–4.2 V, (vs. K/K$^+$), where 1 C = 100 mA g^{-1}, using a programmable battery tester (WonATech, Seoul, Republic of Korea). The galvanostatic intermittent titration technique (GITT) measurements were conducted during 2 cycles of the 0.1 C cycling, in the voltage range of 1.5–3.9 V with each 15 min pulse step, followed by a 1 h relaxation step.

4.4. Computational details

DFT calculations were performed using the Vienna ab initio simulation package (VASP, University of Vienna, Vienna, Austria) [58]. Projector-augmented wave (PAW) pseudopotentials were used with a plane-wave basis set, as implemented in VASP [59]. The Perdew-Burke-Ernzerhof (PBE) parametrization of the generalized gradient approximation (GGA) was used for the exchange-correlation functional [60]. The GGA+U method [61] was adopted to address the localization of the d-orbitals in Cu (U = 4.0 eV) and Mn (U = 3.9 eV), as determined in a previous study [62]. In the DFT calculations, a $6 \times 6 \times 2$ k-point grid was used to calculate $2 \times 3 \times 1$ supercell structure of P3-KMO and P3-KMMCO. Each calculation was performed with an energy cutoff of 500 eV, and each structure was optimized until the force in the unit cell converged to within 0.03 eV Å^{-1}. All K$^+$/vacancy

configurations of each composition were generated based on the cluster expansion method using the cluster-assisted statistical mechanics (CASM) software (University of Michigan, Ann Arbor, MI, USA) [63]. Additionally, the formation energies of the compositions of P3-KMMCO were plotted in the form of a convex hull plot by performing full DFT calculations for up to 20 configurations, with the lowest electrostatic energy of each composition. The Heyd–Scuseria–Ernzerhof (HSE06) hybrid functional was applied to calculate the pDOS (projected density of states) of the Mg, Cu, and O ions [64]. Nudged elastic band (NEB) calculations were performed to predict the activation barrier K$^+$ diffusion within the P3-KMO and P3-KMMCO structures [65]. The diffusion pathways were carried out by generating five intermediate positions based on the fully stable location of the K$^+$ ions. The lattice parameters were fixed, whereas the atomic positions were allowed to be adjusted to accurately determine the adequate intermediate ion positions during the calculation process.

CRediT authorship contribution statement

Yunjae Oh: Writing – original draft, Visualization, Data curation. **Hoseok Lee:** Validation, Software, Resources. **Gwangeon Oh:** Formal analysis, Conceptualization. **Seongje Ryu:** Data curation, Formal analysis. **Un-Hyuck Kim:** Investigation, Data curation. **Hun-Gi Jung:** Formal analysis, Writing – review & editing. **Jongsoon Kim:** Writing – review & editing, Validation, Software. **Jang-Yeon Hwang:** Writing – review & editing, Supervision, Conceptualization.

Declaration of Competing Interest

The authors declare that they have no known competing financial interests or personal relationships that could have appeared to influence the work reported in this paper.

Appendix A. Supplementary data

Supplementary data to this article can be found online at https://doi.org/10.1016/j.jpowsour.2024.235786.

Data availability

No data was used for the research described in the article.

References

[1] B. Scrosati, Paper Powers Battery Breakthrough, Nat. Nanotechnol. 2 (2007) 298–599, https://doi.org/10.1038/nnano.2007.318.

[2] N. Yabuuchi, K. Kubota, M. Dahbi, S. Komaba, Research Development on Sodium-Ion Batteries, Chem. Rev. 14 (2014) 11636–11682, https://doi.org/10.1021/cr500192f.

[3] N. Voronina, Y.-K. Sun, S.-T. Myung, Co-Free Layered Cathode Materials for High Energy Density Lithium-Ion Batteries, ACS Energy Lett 5 (2020) 1814–1824, https://doi.org/10.1021/acsenergylett.0c00742.

[4] C.B.L. Nkulu, L. Casas, V. Haufroid, T.D. Putter, N.D. Saenen, T.K. Kitenge, P. M. Obadia, D.K.W. Mukoma, J.-M.L. Ilunga, T.S. Nawrot, O.L. Numbi, E. Smolders, B. Nemery, Sustainability of Artisanal Mining of Cobalt in DR Congo, Nat. Sustain. 1 (2018) 495–504, https://doi.org/10.1038/s41893-018-0139-4.

[5] K. Turcheniuk, D. Bondarev, V. Singhal, G. Yushin, Ten Year Left to Redesign Lithium-Ion Batteries, Nature 559 (2018) 467–470, https://doi.org/10.1038/d41586-018-05752-3.

[6] J.-Y. Hwang, S.-T. Myung, Y.K. Sun, Sodium-Ion Batteries: Present and Future, Chem. Soc. Rev. 46 (2017) 3529–3614, https://doi.org/10.1039/C6CS00776G.

[7] X. Liang, J.-Y. Hwang, Y.-K. Sun, Practical Cathode for Sodium-Ion Batteries: Who Will Take The Crown? Adv. Energy Mater. 13 (2023) 2310975 https://doi.org/10.1002/aenm.202301975.

[8] A. Manthiram, Y. Fu, S.-H. Chung, C. Zu, Y.-S. Su, Rechargeable Lithium–Sulfur Batteries, Chem. Rev. 114 (2014) 11751–11787, https://doi.org/10.1021/cr500062v.

[9] Y. Du, Z. Zhang, Y. Xu, J. Bao, X. Zhou, Metal Sulfide-Based Potassium-Ion Battery Anodes: Storage Mechanisms and Synthesis Strategies, Acta Phys. Chim. Sin. 38 (2022) 2205017, https://doi.org/10.3866/PKU.WHXB202205017.

[10] Y. Xu, U. Du, H. Chen, J. Chen, T. Ding, D. Sun, D.H. Kim, Z. Lin, X. Zhou, Recent Advances in Rational Design for High-Performance Potassium-Ion Batteries, Chem. Soc. Rev. 53 (2024) 7202, https://doi.org/10.1039/D3CS00601H.

[11] L. Liu, J. Liang, W. Wang, C. Han, Q. Xia, X. Ke, J. Liu, Q. Gu, Z. Shi, S. Chou, S. Dou, W. Li, A P3-Type $K_{1/2}Mn_{5/6}Mg_{1/12}Ni_{1/12}O_2$ Cathode for Potassium-Ion Batteries with High Structural Reversibility Secured by the Mg–Ni Pinning Effect, ACS Appl. Mater. Interfaces 13 (2021) 28369–28377, https://doi.org/10.1021/acsami.1c07220.

[12] J.-Y. Hwang, S.-T. Myung, Y.-K. Sun, Recent Progress in Rechargeable Potassium Batteries, Adv. Funct. Mater. 28 (2018) 1802938, https://doi.org/10.1002/adfm.201802938.

[13] X. Wang, P. Hu, C. Niu, J. Meng, X. Xu, X. Wei, C. Tang, W. Luo, L. Zhou, Q. An, L. Mai, New-Type $K_{0.7}Fe_{0.5}Mn_{0.5}O_2$ Cathode with an Expanded and Stabilized Interlayer Structure for High-Capacity Sodium-Ion Batteries, Nano Energy 35 (2017) 71–78, https://doi.org/10.1016/j.nanoen.2017.03.026.

[14] C. Deng, X. Li, R. Chen, K. Ye, J. Lipton, S.A. Maclean, H. Wang, A.D. Taylor, G. M. Weng, Recent Advances in Rocking Chair Batteries and Beyond, Energy Storage Mater 60 (2023) 102820, https://doi.org/10.1016/j.ensm.2023.102820.

[15] A. Manthiram, A Reflection on Lithium-Ion Battery Cathode Chemistry, Nat. Commun. 11 (2020) 1550, https://doi.org/10.1038/s41467-020-15355-0.

[16] L. Li, Z. Hu, Q. Liu, J.-Z. Wang, Z. Guo, H.-K. Liu, Cathode Materials for High-Performance Potassium-Ion Batteries, Cell Rep 2 (2021) 100657, https://doi.org/10.1016/j.xcrp.2021.100657.

[17] H. Kim, D.-H. Seo, J.C. Kim, S.-H. Bo, L. Liu, T. Shi, G. Ceder, Investigation of Potassium Storage in Layered P3-Type $K_{0.5}MnO_2$ Cathode, Adv. Mater. 29 (2017) 1702480, https://doi.org/10.1002/adma.201702480.

[18] H. Kim, J.C. Kim, S.-H. Bo, T. Shi, D.-H. Kwon, G. Ceder, K-Ion Batteries Based on a P2-Type $K_{0.6}CoO_2$ Cathode, Adv. Energy Mater. 7 (2017) 1700098, https://doi.org/10.1002/aenm.201700098.

[19] J.-Y. Hwang, J. Kim, T.-Y. Yu, S.-T. Myung, Y.-K. Sun, Development of P3-$K_{0.69}CrO_2$ as an Ultra-High-Performance Cathode Material for K-Ion Batteries, Energy Environ. Sci. 11 (2018) 2821–2827, https://doi.org/10.1039/C8EE01365A.

[20] L. Deng, X. Niu, G. Ma, Z. Yang, L. Zeng, Y. Zhu, L. Guo, Layered Potassium Vanadate $K_{0.5}V_2O_5$ as a Cathode Material for Nonaqueous Potassium Ion Batteries, Adv. Funct. Mater. 28 (2018) 18006470, https://doi.org/10.1002/adfm.201800670.

[21] L. Duan, C. Shao, J. Liao, L. Song, Y. Zhang, R. Li, S. Guo, X. Zhou, H. Zhou, A P2/P3 Biphasic Layered Oxide Composite as a High-Energy and Long-Cycle-Life Cathode for Potassium-Ion Batteries, Angew. Chem. Int. Ed. 63 (2024) e202400868, https://doi.org/10.1002/anie.202400868.

[22] M.A. Halcrow, Jahn–Teller Distortions in Transition Metal Compounds, and Their Importance in Functional Molecular and Inorganic Materials, Chem. Soc. Rev. 42 (2013) 1784–1795, https://doi.org/10.1039/C2CS35253B.

[23] Y. Kim, G. Oh, J. Lee, H. Kang, H. Kim, J. Park, S. Kansara, J.-Y. Hwang, Y. Park, K. R. Lestari, T.-H. Kim, J. Kim, Stabilization of Layered-Type Potassium Manganese Oxide Cathode with Fluorine Treatment for High-Performance K-Ion Batteries, J. Power Sources 588 (2023) 233729, https://doi.org/10.1016/j.jpowsour.2023.233729.

[24] Z. Xiao, F. Xia, L. Xu, X. Wang, J. Meng, H. Wang, X. Zhang, L. Geng, J. Wu, L. Mai, Suppressing the Jahn–Teller Effect in Mn-Based Layered Oxide Cathode toward Long-Life Potassium-Ion Batteries, Adv. Funct. Mater. 32 (2021) 2108244, https://doi.org/10.1002/adfm.202108244.

[25] Z. Xiao, J. Meng, F. Xia, J. Wu, F. Liu, X. Zhang, L. Xu, X. Lin, L. Mai, K^+ Modulated K^+/Vacancy Disordered Layered Oxide for High-Rate and High-Capacity Potassium-Ion Batteries, Energy Environ. Sci. 13 (2020) 3129–3137, https://doi.org/10.1039/D0EE01607A.

[26] M.G.T. Nathan, N. Naveen, W.B. Park, K.-S. Sohn, M. Pyo, Fast Chargeable P2–K$_{-2/3}$[Ni$_{1/3}$Mn$_{2/3}$]O$_2$ for Potassium Ion Battery Cathodes, J. Power Sources 438 (2019) 226992, https://doi.org/10.1016/j.jpowsour.2019.226992.

[27] R.-J. Luo, X.-L. Li, J.-Y. Ding, J. Bao, C. Ma, C.-Y. Du, X.-Y. Cai, X.-J. Wu, Y.-N. Zhou, Suppressing Jahn–Teller Distortion and Phase Transition of $K_{0.5}MnO_2$ by K-Site Mg Substitution for Potassium-Ion Batteries, Energy Storage Mater 47 (2022) 408–414, https://doi.org/10.1016/j.ensm.2022.02.027.

[28] C.-L. Liu, S.-H. Luo, H.-B. Huang, X. Liu, Y.-C. Zhai, Z.-W. Wang, Fe-Doped Layered P3-Type $K_{0.45}Mn_{1-x}Fe_xO_2$ (x ≤ 0.5) as Cathode Materials for Low-Cost Potassium-Ion Batteries, Chem. Eng. J. 378 (2019) 122167, https://doi.org/10.1016/j.cej.2019.122167.

[29] J.U. Choi, J. Kim, J.-Y. Hwang, J.H. Jo, Y.-K. Sun, S.-T. Myung, $K_{0.54}[Co_{0.5}Mn_{0.5}]O_2$: New Cathode with High Power Capability for Potassium-Ion Batteries, Nano Energy 61 (2019) 284–294, https://doi.org/10.1016/j.nanoen.2019.04.062.

[30] P. Bai, K. Jiang, X. Zhang, J. Xu, S. Guo, H. Zhou, Ni-Doped Layered Manganese Oxide as a Stable Cathode for Potassium-Ion Batteries, ACS Appl. Mater. Interfaces 12 (2020) 10490–10495, https://doi.org/10.1021/acsami.9b22237.

[31] S. Park, S. Park, Y. Park, M.H. Alfaruqi, J.-Y. Hwang, J. Kim, A New Material Discovery Platform of Stable Layered Oxide Cathodes for K-Ion Batteries, Energy Environ. Sci. 14 (2021) 5864–5874, https://doi.org/10.1039/D1EE01136G.

[32] X. Zhang, D. Yu, Z. Wei, N. Chen, G. Chen, Z.X. Shen, F. Du, Layered P3-Type $K_{0.4}Fe_{0.1}Mn_{0.8}Ti_{0.1}O_2$ as a Low-Cost and Zero-Strain Electrode Material for Both Potassium and Sodium Storage, ACS Appl. Mater. Interfaces 13 (2021) 18897–18904, https://doi.org/10.1021/acsami.1c03233.

[33] G. Li, Z. Huang, J. Chen, F. Yao, J. Liu, O.L. Li, S. Sun, Z. Shi, Rechargeable Zn-Ion Batteries with High Power and Energy Densities: A Two-Electron Reaction Pathway in Birnessite MnO_2 Cathode Materials, J. Mater. Chem. A. 8 (2020) 1975–1985, https://doi.org/10.1039/C9TA11985J.

[34] J. Lv, B. Wang, J. Hao, H. Ding, L. Fan, R. Tao, H. Yang, J. Zhou, B. Lu, Single-Crystalline Mn-Based Oxide as a High-Rate and Long-Life Cathode Material for Potassium-Ion Battery, eScience 3 (2023) 100081, https://doi.org/10.1016/j.esci.2022.10.007.

[35] J. Liang, C. Lin, X. Meng, M. Liang, J. Lai, X. Zheng, Q. Huang, L. Liu, Z. Shi, P3-Type $K_{0.45}Co_{1/12}Mg_{1/12}Mn_{5/6}O_2$ as a Superior Cathode Material for Potassium-Ion Batteries with High Structural Reversibility Ensured by Co–Mg co-substitution, J. Mater. Chem. A. 9 (2021) 17261–17269, https://doi.org/10.1039/D1TA05579H.

[36] W. Kong, R. Gao, Q. Li, W. Yang, J. Yang, L. Sun, X. Liu, Simultaneously Tuning Cationic and Anionic Redox in a P2-$Na_{0.67}Mn_{0.75}Ni_{0.25}O_2$ Cathode Material through Synergic Cu/Mg Co-Doping, J. Mater. Chem. A 7 (2019) 9099–9109, https://doi.org/10.1039/C9TA00968J.

[37] H. Chen, X.-W. Gao, Q. Li, R.-Z. Niu, S.-S. Wang, Q.-F. Gu, J.-J. Mu, W.-B. Luo, Layer-Structured $K_{0.5}Mn_{0.8}Cu_{0.1}Mg_{0.1}O_2$ for High-Performance Potassium-Ion Batteries by Alleviating the Phase Transformation, J. Mater. Chem. A 12 (2024) 6261–6268, https://doi.org/10.1039/d4ta00423j.

[38] Y. Zheng, H. Xie, J. Li, K.S. Hui, Z. Yu, H. Xu, D.A. Dinh, Z. Ye, C. Zha, K.N. Hui, Insights into the Jahn–Teller Effect in Layered Oxide Cathode Materials for Potassium-Ion Batteries, Adv. Energy Mater. 14 (2024) 2400461, https://doi.org/10.1002/aenm.202400461.

[39] C.-L. Liu, S.-H. Luo, H.-B. Huang, Y.-C. Zhai, Z.-W. Wang, Low-Cost Layered $K_{0.45}Mn_{0.9}Mg_{0.1}O_2$ as a High-Performance Cathode Material for K-Ion Batteries, ChemElectroChem 6 (2019) 2308–2315, https://doi.org/10.1002/celc.201900326.

[40] J. Weng, J. Duan, C. Sun, P. Liu, A. Li, P. Zhou, J. Zhou, Construction of Hierarchical $K_{0.7}Mn_{0.7}Mg_{0.3}O_2$ Microparticles as High Capacity & Long Cycle Life Cathode Materials for Low-Cost Potassium-Ion Batteries, Chem. Eng. J. 392 (2020) 123649, https://doi.org/10.1016/j.cej.2019.123649.

[41] C. Zhao, F. Ding, Y. Lu, L. Chen, Y.-S. Hu, High-Entropy Layered Oxide Cathodes for Sodium-Ion Batteries, Angew. Chem. Int. Ed. 59 (2019) 264–269, https://doi.org/10.1002/anie.201912171.

[42] J. Gild, Y. Zhang, T. Harrington, S. Jiang, T. Hu, M.C. Quinn, W.M. Mellor, N. Zhou, K. Vecchio, J. Luo, High-Entropy Metal Diborides: A New Class of High-Entropy Materials and a New Type of Ultrahigh Temperature Ceramics, Sci. Rep. 6 (2016) 37946, https://doi.org/10.1038/srep37946.

[43] B.S. Kumar, A. Pradeep, V. Srihari, H.K. Poswal, R. Kumar, A. Amardeep, A. Chatterjee, A. Mukhopadhyay, Cation–Oxygen Bond Covalency: A Common Thread and a Major Influence toward Air/Water-Stability and Electrochemical Behavior of "Layered" Na–Transition-Metal-Oxide-Based Cathode Materials, Adv. Energy Mater. 13 (2023) 2204407, https://doi.org/10.1002/aenm.202204407.

[44] C. Zhao, Q. Wang, Z. Yao, J. Wang, B.S. Lengeling, F. Ding, X. Qi, Y. Lu, X. Bai, B. Li, H. Li, A.A. Guzik, X. Huang, C. Delmas, M. Wagemaker, L. Chen, Y.-S. Hu, Rational Design of Layered Oxide Materials for Sodium-Ion Batteries, Science 370 (2020) 708–711, https://doi.org/10.1126/science.aay9972.

[45] S. Li, L. Wu, H. Fu, A.M. Rao, L. Cha, J. Zhou, B. Lu, Entropy-Tuned Layered Oxide Cathodes for Potassium-Ion Batteries, Small Methods 7 (2023) 2300893, https://doi.org/10.1002/smtd.202300893.

[46] F. Ding, C. Zhao, D. Xiao, X. Rong, H. Wang, Y. Li, Y. Yang, Y. Lu, Y.-S. Hu, Using High-Entropy Configuration Strategy to Design Na-Ion Layered Oxide Cathodes with Superior Electrochemical Performance and Thermal Stability, J. Am. Chem. Soc. 144 (2022) 8286–8295, https://doi.org/10.1021/jacs.2c02353.

[47] Y. Yokoyama, D. Outsuki, T. Sugimoto, H. Wadati, J. Okabayashi, X. Yang, F. Du, G. Chen, T. Mizokawa, Electronic structure of Li$_{1+x}$[Mn$_{0.5}$Ni$_{0.5}$]$_{1-x}$O$_2$ studied by photoemission and x-ray absorption spectroscopy, Appl. Phys. Lett. 107 (2015) 033903, https://doi.org/10.1063/1.4927239.

[48] Y. Huang, X. Zhang, H. Lin, Z. Wei, Y. Zeng, X. Ge, W. Zhang, X. Wang, X. Jin, Z. X. Shen, F. Du, Synergistically Enhanced Structural, Thermal and Interfacial Stability of $K_{0.45}MnO_2$ via Tailoring the Local Structure for High-Energy and High-Power Potassium-Ion Batteries, Chem. Eng. J. 453 (2023) 139571, https://doi.org/10.1016/j.cej.2022.139571.

[49] X. Liang, T.-Y. Yu, H.-H. Ryu, Y.-K. Sun, Hierarchical O3/P2 Heterostructured Cathode Materials for Advanced Sodium-Ion Batteries, Energy Storage Materials 47 (2022) 515–525, https://doi.org/10.1016/j.ensm.2022.02.043.

[50] D.W. Dees, S. Kawauchi, D.P. Abraham, J. Prakash, Analysis of the Galvanostatic Intermittent Titration Technique (GITT) as Applied to a Lithium-Ion Porous Electrode, J. Power Sources 189 (2009) 263–268, https://doi.org/10.1016/j.jpowsour.2008.09.045.

[51] Y. Jeong, H.-J. Shin, M.H. Alfaruqi, M.S. Ahmed, V. Mathew, H.-G. Jung, J. Kim, J.-Y. Hwang, A nitrogen-doped amorphous/graphitic hybrid carbon material derived from a sustainable resource for low-cost K-ion battery anodes, J. Mater. Chem. A 10 (2022), https://doi.org/10.1039/D2TA04195B.

[52] G. Oh, S. Kansara, X. Xu, Y. Lu, J.-Y. Hwang, S. Xiong, J.-Y. Hwang, Stabilizing Layered-Type $K_{0.4}V_2O_5$ Cathode by K Site Substitution with Strontium for K-Ion Batteries, Adv. Funct. Mater. 34 (2024) 2401210, https://doi.org/10.1002/adfm.202401210.

[53] P. Pallavicini, G. Dacarro, P. Grisoli, C. Mangano, M. Patrini, F. Rigoni, L. Sangaletti, A. Taglietti, Coordination Chemistry for Antibacterial Materials: a

Monolayer of a Cu^{2+} 2,2'-Bipyridine Complex Grafted on a Glass Surface, Dalton Trans 42 (2013) 4552–4560, https://doi.org/10.1039/c2dt32607h.

[54] J.-Y. Hwang, J. Kim, T.-Y. Yu, H.-G. Jung, J. Kim, K.-H. Kim, Y.-K. Sun, A New P2-Type Layered Oxide Cathode with Superior Full-Cell Performances for K-Ion Batteries, J. Mater. Chem. A 7 (2019) 21362–21370, https://doi.org/10.1039/C9TA07837A.

[55] R. Berthelot, D. Carlier, C. Delmas, Electrochemical Investigation of the P2–Na_xCoO_2 Phase Diagram, Nat. Mater. 10 (2011) 74–80, https://doi.org/10.1038/nmat2920.

[56] J.-U. Choi, J. Kim, J.-H. Jo, H.-J. Kim, Y.-H. Jung, D.-C. Ahn, Y.-K. Sun, S.-T. Myung, Facile Migration of Potassium Ions in a Ternary P3-Type $K_{0.5}[Mn_{0.8}Fe_{0.1}Ni_{0.1}]O_2$ Cathode in Rechargeable Potassium Batteries, Energy Storage Mater 25 (2020) 714–723, https://doi.org/10.1016/j.ensm.2019.09.015.

[57] C. Cheng, C. Chen, S. Chu, H. Hu, T. Yan, X. Xia, X. Feng, J. Guo, D. Sun, J. Wu, S. Guo, L. Zhang, Enhancing the Reversibility of Lattice Oxygen Redox Through Modulated Transition Metal–Oxygen Covalency for Layered Battery Electrodes, Adv. Mater. 34 (2022) 2201152, https://doi.org/10.1002/adma.202201152.

[58] G. Kresse, J. Furthmüller, Efficiency of Ab-Initio Total Energy Calculations for Metals and Semiconductors Using a Plane-Wave Basis Set, Comput. Mater. Sci. 6 (1996) 15–50, https://doi.org/10.1016/0927-0256(96)00008-0.

[59] P.-E. Blöchl, Projector Augmented-Wave Method, Phys. Rev. B 50 (1994) 17953–17979, https://doi.org/10.1103/PhysRevB.50.17953.

[60] J.-P. Perdew, K. Burke, M. Ernzerhof, Generalized Gradient Approximation Made Simple, Phys. Rev. Lett. 77 (1996) 3865–3868, https://doi.org/10.1103/PhysRevLett.77.3865.

[61] V.-I. Anisimov, F. Aryasetiawan, A.-I. Lichtenstein, First-Principles Calculations of the Electronic Structure and Spectra of Strongly Correlated Systems: the LDA+ U Method, J. Phys.: Condens. Matter 9 (1997) 767, https://doi.org/10.1088/0953-8984/9/4/002.

[62] A. Jain, G. Hautier, S.-P. Ong, C.-J. Moore, C.-C. Fischer, K.-A. Persson, G. Ceder, Formation Enthalpies by Mixing GGA and GGA + U Calculations, Phys. Rev. B 84 (2011) 045115, https://doi.org/10.1103/PhysRevB.84.045115.

[63] A. Van der Ven, J.C. Thomas, Q. Xu, J. Bhattacharya, Linking the Electronic Structure of Solids to Their Thermodynamic and Kinetic Properties, Math. Comput. Simul. 80 (2010) 1393–1410, https://doi.org/10.1016/j.matcom.2009.08.008.

[64] J. Heyd, G.-E. Scuseria, M. Ernzerhof, Hybrid Functionals Based on a Screened Coulomb Potential, J. Chem. Phys. 118 (2003) 8207–8215, https://doi.org/10.1063/1.1564060.

[65] G. Henkelman, B.-P. Uberuaga, H. Jónsson, A Climbing Image Nudged Elastic Band Method for Finding Saddle Points and Minimum Energy Paths, J. Chem. Phys. 113 (2000) 9901–9904, https://doi.org/10.1063/1.1329672.